A Multi-rule-based Relative Radiometric Normalization for Multi-Sensor Satellite Images

Hanzeyu Xu, Yuyu Zhou, Yuchun Wei, Houcai Guo, and Xiao Li

***Abstract*—Relative radiometric normalization (RRN) is a widely used method for enhancing the radiometric consistency among multi-temporal satellite images. Diverse satellite images enhance the information for observing the Earth's surface and bring additional uncertainties in the applications using multi-sensor images, such as change detection, multi-temporal analysis, image fusion, etc. To address this challenge, we developed a multi-rule-based RRN method for multi-sensor satellite images, which involves the identification of spectral- and spatial-invariant pseudo-invariant features (PIFs) and a Partial least-squares (PLS) regression-based RRN modeling using neighboring target pixels around PIFs. The proposed RRN method was validated on four datasets and demonstrated excellent effectiveness in identifying high-quality PIFs with spectral- and spatial-invariant properties, estimating precise regression models, and enhancing the radiometric consistency of reference-target image pair. Our method outperformed six RRN methods and effectively processed well-registered medium- and high-resolution images from the same sensor. This letter highlights the potential of our method for generating more comparable bi-temporal multi-sensor images.**

***Index Terms*—Relative radiometric normalization (RRN), pseudo-invariant features (PIFs), log-Gabor filter, multi-sensor images, Partial least-squares (PLS), radiometric consistency.**

I. INTRODUCTION

RADIOMETRIC normalization is an essential pre-processing step for reducing radiometric inconsistency among multi-temporal satellite observations caused by changes in sensor calibration, illumination, viewing angle, atmospheric conditions, and ground properties over time [1]. While absolute radiometric normalization (ARN) methods convert image digital numbers to physical surface reflectance values using complex atmospheric correction models, relative radiometric normalization (RRN) methods are commonly used to adjust the radiometric properties of a target image to match those of a reference image [2].

This work was supported in part by the National Natural Science Foundation of China under Grant 42271342 and 41471283, and the program of the China Scholarship Council under Grant 202006860054. (Corresponding author: Yuyu Zhou; Yuchun Wei.)

H. Xu, Y. Wei, and H. Guo are with the Jiangsu Center for Collaborative Innovation in Geographical Information Resource Development and Application, Key Laboratory of Virtual Geographic Environment (Nanjing Normal University), Ministry of Education, and School of Geography, Nanjing Normal University, Nanjing 210023, China (e-mail: xuhanzeyu@njnu.edu.cn; weiyuchun@njnu.edu.cn; guohoucai@nnu.edu.cn.).

Y. Zhou is with the Department of Geography, The University of Hong Kong, Hong Kong 999077, China (e-mail: yuyuzhou@hku.hk).

X, Li is with the Transport Studies Unit, University of Oxford, Oxford OX1 3QY, United Kingdom (e-mail: xiao.li@ouce.ox.ac.uk).

Digital Object Identifier

RRN can be classified into dense RRN (DRRN) and sparse RRN (SRRN) methods based on pixel pairs used to establish the radiometric distortion relationship of radiometric features between a reference-target image pair [3]. DRRN methods determine the adjustment of radiometric properties using all pixels of the reference and target images without considering differences caused by land cover changes and radiometric distortion, such as Haze correction (HC), Minimum-maximum (MM) normalization, Simple regression (SR), and Histogram matching (HM) [1]. Comparatively, SRRN methods apply identified time-invariant pixels with invariant or near-invariant radiance, known as pseudo-invariant features (PIFs), to establish the radiometric transforming model for a reference-target image pair, and then normalize the target image [4].

The identification of PIFs is crucial for implementing SRRN methods. To ensure the quality of PIFs, PIFs identification methods have been developed from manual or semi-automatic selection to math transformation methods represented by multi-version Multivariate alteration detection (MAD) [5] and Iterative slow feature analysis (ISFA) [6]. Radiometric distortion adjustment is essential for high-resolution and multi-sensor images in various remote sensing applications, as its capability of improving the performance of change detection, classification, and mosaicking [7]. Aided by stepwise spatial and spectral metrics, multi-rule-based SRRN methods have been shown to perform better in identifying robust PIFs with steady physical properties of land covers from well-registered high-resolution images [8, 9]. However, the impacts of local mismatches on PIFs and RRN modeling still need to be considered [10]. Keypoint-descriptor-based SRRN methods have the potential to identify PIFs insensitive to geometric and radiation distortions in unregistered images [3, 11, 12]. These methods only rely on the blob- or corner-based descriptors and weaken the use of spectral information in high-resolution images, leading to potential uncertainties in RRN results. To address this issue, a tensor-based keypoint detection method has been proposed to preserve both spatial and spectral information over all bands for more reliable PIFs identification [13]. However, its complexity may restrict the application for various high-resolution images.

Diverse multi-spectral images record the Earth's surface at different spatial resolutions and coverage ranges, providing valuable observations for applications requiring higher spatial, temporal, and spectral details. However, radiances distortion caused by acquisition system differences brings uncertainties in application results. Radiometric inconsistency persists in multi-sensor images even after using ARN due to atmospheric correction modeling biases [7]. Thus, integrating RRN and

ARN has proven to be advantageous to produce harmonized results with consistent physical meanings [7, 14], which can facilitate the applications of multi-sensor images, such as change detection, multi-temporal analysis, and image fusion.

To reduce uncertainties from the inconsistent radiance and result in more comparable bi-temporal multi-sensor images for wider applications, in this letter, we proposed a multi-rule-based RRN method for multi-sensor satellite images. The main contributions include: 1) we developed a spectral- and spatial-invariant PIFs identification using the measurements robust to local mismatches and radiation variation; 2) we estimated the radiometric transforming models by considering the neighboring target pixels centered on the identified PIFs. The remainder of this letter is organized as follows: Section II details the proposed method; Section III reports and analyzes experimental results; and Section IV draws conclusions.

II. Methodology

The proposed method includes spectral- and spatial-invariant PIFs identification and RRN modeling using Partial least-squares (PLS) regression [15] (Fig. 1). First, we identified PIFs by measuring the pixels invariant to both spectral and spatial distortions. Then, we used PLS regression to estimate the (target) group-to-(reference) pixel relationships between the image pair for normalizing the target image.

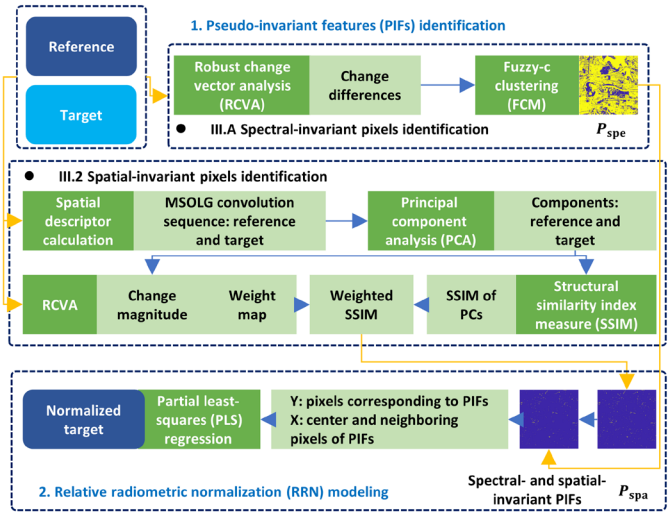

Fig. 1 Flowchart of the proposed method.

A. Spectral-Invariant Pixels Identification

To accurately identify spectral-invariant pixels and account for the effects of local mismatch and high building shadows, we used Robust change vector analysis (RCVA) [16] to obtain differences in each band between reference and target images (1-2). Then, we used the Fuzzy-C clustering (FCM) algorithm to classify the band differences into two clusters and used the unchanged part as spectral-invariant pixels, denoted as P_{spe}.

$$\begin{aligned} Diffa_i(j,k) &= \min\{(R_i(j,k) - T_i(p,q)) \geq 0\}, \\ Diffb_i(j,k) &= \min\{(T_i(j,k) - R_i(p,q)) \geq 0\}, \\ p &\in [j-w, j+w], q \in [k-w, k+w], \end{aligned} \quad (1)$$

$$Diff_i(j,k) = \begin{cases} Diffa_i > 0 \rightarrow Diffa_i \\ Diffa_i = 0 \rightarrow 0 - Diffb_i \end{cases} \quad (2)$$

where R_i and T_i is the ith band of reference and target. we used $w = 1$ for a 3 × 3 moving window.

B. Spatial-Invariant Pixels Identification

First, we generated spatial features for both reference and target images using Multi-scale and multi-oriented log-Gabor (MSOLG) filters, which are insensitive to radiation variation. Then, we used the main component pairs of MSOLG features to calculate the weighted Structural similarity index measure (SSIM) for reference and target images. Finally, we identified the pixels with higher similarity in each weighted SSIM map as candidate spatial-invariant pixels. The spatially intersecting pixels of all candidate layers were determined as spatial-invariant pixels using majority voting.

1) MSOLG Feature Extraction: The 2-D log-Gabor wavelet in the spatial domain is defined by applying the inverse Fourier transform. The real and imaginary components of the filter refer to even-symmetric and odd-symmetric log-Gabor wavelets, denoted as L^{even} and L^{odd}. The convolution results of an input image $I(x,y)$ are regarded as a response vector as follows [17]:

$$\begin{aligned} &[E_{so}(x,y), O_{so}(x,y)] = \\ &[I(x,y) \times L^{even}(x,y,s,o), I(x,y) \times L^{odd}(x,y,s,o)] \end{aligned} \quad (3)$$

where $E_{so}(x,y)$ and $O_{so}(x,y)$ is the response of L^{even} and L^{odd} at scale s and orientation o. Image display in standard false color is used as $I(x,y)$. Then, the amplitude component $A_{so}(x,y)$ of $I(x,y)$ at s and o is calculated as,

$$A_{so}(x,y) = \sqrt{E_{so}(x,y)^2 + O_{so}(x,y)^2} \quad (4)$$

We used the sum of $A_{so}(x,y)$ over all scales s to represent the log-Gabor layers $A_o(x,y)$ for each orientation o:

$$A_o(x,y) = \sum_{n=1}^{N_s} A_{so}(x,y), s = 1,2,..,N_s \quad (5)$$

The number of s and o were denoted as N_s and N_o. We obtained N_o MSOLG features for a reference or target image.

2) Weighted SSIM Calculation: To avoid excessive diversity resulting from MSOLG features with multiple orientations in identifying candidate spatial-invariant pixels, we first used Principal component analysis (PCA) to extract the main information from the MSOLG features of reference and target images. Next, we selected the first four main components that contain over 95% of the total information to compute SSIM and depict the spatial structural similarity between the reference and target images. It should be noted that the image pair exhibits similar structures after co-registration, resulting in a large number of pixels with higher SSIM values. Selecting pixels with higher SSIM values directly as candidate spatial-invariant pixels leads to an imbalanced pixel allocation and generates the PIFs that lack representativeness. Therefore, we introduced a spatial difference-based weight image to adjust the histogram distribution of SSIM maps. This weight image was computed using the change magnitude (m_{spa}) between all component pairs of the MSOLG features,

$$m_{spa} = \sqrt{\sum_{i=1}^{n} \left(Diff_{Mi}(j,k)\right)^2} \quad (6)$$

where $Diff_{Mi}$ is the RCVA-based difference between the ith

MSOLG feature component pair (1-2). The weight image was obtained as,

$$w = e^{-0.2 \times m_{spa}} \tag{7}$$

Then, SSIM maps of four main components ($SSIM_{\mathrm{PC}_n}, n = 1, 2, 3, 4$) were updated as:

$$wSSIM_{\mathrm{PC}_n} = w \odot SSIM_{\mathrm{PC}_n} \tag{8}$$

3) Spatial-Invariant Pixels Identification: First, we selected the top 10% of pixels with significant similarity from $wSSIM_{\mathrm{PC}_n}$ as candidate spatial-invariant pixels (C_{PC_n}). Then, we used majority voting to identify the spatial-invariant pixels (P_{spa}) from the binarized C_{PC_n},

$$P_{\mathrm{spa}} = \begin{cases} 1, \text{if } \sum_{n=1}^{n} C_{\mathrm{PC}_n} > \frac{n}{2} \\ 0, \text{if } \sum_{n=1}^{n} C_{\mathrm{PC}_n} \le \frac{n}{2} \end{cases} \tag{9}$$

where n is the number of selected main components. We used the spatial intersection parts of P_{spe} and P_{spa} as the spectral- and spatial-invariant PIFs.

C. RRN Modeling Using PLS Regression

Geographic variables are mutually related to each other in spatial distribution [18]. As the spatial resolution increases, satellite sensors can better detail ground objects, leading to stronger correlations among pixels. To eliminate the impacts of local mismatch and fully use correlative pixel information in a high-resolution image, we performed a (target) group-to-(reference) pixel RRN modeling instead of the conventional pixel-to-pixel method. For each band, neighboring pixels centered on PIFs in the target image were also involved to fit the pixels corresponding to PIFs in the reference image. Considering the impact of collinearity among multi-dimension variables on the regression model, we used PLS regression to estimate radiometric transforming models between predictor combinations with the most uncorrelated components and response values. A window of 3 × 3 pixels was used to build nine-dimension predictor variables. To ensure the percentage of the variance explained in the response variables, we used the first four PLS components to estimate the models of each band.

D. Evaluation metric

1) Evaluation of the identified PIFs: the quality of PIFs was qualitatively assessed using visual checking and quantitatively evaluated through calculating Pearson correlation coefficient r of PIFs in each band [4].

2) Evaluation of RRN performance: for measuring the precision of the regression model, we used 10-fold cross-validation to calculate Root mean squared error (RMSE) and coefficient of determination (R^2). For evaluating RRN performance, the differences between reference-target image pairs before and after applying the RRN were compared via 1) checkerboard visualization showing the improvement in image brightness intensity difference, and 2) the changes of average RMSE belonging to the unchanged area and the Peak signal-to-noise ratio (PSNR) of the entire image.

$$\mathrm{RMSE}_{\mathrm{Ave.}}{}^{b} = \sqrt{\frac{1}{n}\sum_{i=1}^{n}\left(R_i{}^{b} - T_i{}^{b}\right)^2} \tag{10}$$

where $\mathrm{RMSE}_{\mathrm{Ave.}}{}^{b}$ is the average RMSE of the bth band. n is the number of unchanged pixels corresponding to P_{spe}. $R_i{}^{b}$ and $T_i{}^{b}$ represent the value of the ith pixel in the bth band of the reference and normalized target images. Lower RMSE and higher PSNR values indicate higher accuracy of the RRN.

III. Experimental Results And Analysis

A. Datasets

The datasets include four-group multi-sensor image pairs for verifying the proposed method and three-group well-registered image pairs from the same sensor for validating the method's applicability. For datasets 1-4, Sentinel-2 MSI L2A products are atmospherically corrected surface reflectance orthoimages and were used as reference images. All Gaofen-2 PMS images were atmospherically corrected using FLAASH and registered to resampled Sentinel-2 MSI images (4 m). Each image pair has various acquisition date span (TABLE I).

B. Identified PIFs

In datasets 1-4, we identified 14,269, 11,687, 12,127, and 14,414 spectral- and spatial-invariant pixels as PIFs (Fig. 2). The identified PIFs exhibited good representativeness and were distributed in areas without land cover changes. The measurements showed that PIFs are of high quality, with mean r of 0.9395, 0.9265, 0.9219, and 0.9084 for each dataset (TABLE II).

Spectral-invariant pixel identification effectively identified unchanged pixels with stable land cover attributes. Moreover, spatial-invariant pixel identification played a crucial role in filtering out the satisfied PIFs from P_{spe}. Extracting MSOLG convolution sequences is an essential step in identifying P_{spa}, the optimal settings for two important parameters N_s and N_o of the log-Gabor filter were determined via a parameter study. Generally, N_s and N_o are the constant greater than 1 and 3, respectively, and increasing N_o lead to more detailed spatial

TABLE I
Data Information

Dataset	Reference / Target						
	Sensor	Spatial resolution	Data type	Band	Date	Size	Location
1	Sentinel-2 MSI/ GaoFen-2 PMS	10 m / 4 m	L2A surface reflectance / L1A Digital Number	Blue, green, red, NIR	2019-09-22 / 2020-02-09	1200×1200	Wuhan
2					2020-03-15 / 2020-02-09		
3					2019-12-04 / 2019-10-19		
4					2019-12-11 / 2018-11-28		
5	Sentinel-2 MSI	10 m	L2A surface reflectance		2020-02-09 / 2019-11-11	1200×1200	
6	Landsat-8 OLI	30 m	C1L2 surface reflectance		2016-12-09 / 2020-12-20	1100×1100	Nanjing
7	TripleSat-2	4 m	Top of atmosphere reflectance		2016-11-27 / 2017-07-18	800×600	

information but higher computational complexity [17]. We performed 20 groups of experiments with different parameters to determine the optimal parameter setting that yielded the highest mean r value for the identified PIFs (TABLE III). The selected parameter setting of N_s = 2 and N_o = 6 was adopted for all datasets in this letter. Furthermore, after incorporating spatial differences into the weight maps, the histogram distribution of raw SSIM values was well-balanced, resulting in a more concentrated distribution of values around zero and fewer values exceeding 0.5 (Fig. 3). It ensured that the pixels with the most significant similarity in $wSSIM_{\mathrm{pc}_n}$ were identified as C_{pc_n}, reducing impacts of insensitiveness of SSIM to local changes.

TABLE II
THE CORRELATION COEFFICIENT OF THE IDENTIFIED PIFS

Band	Dataset-1	Dataset-2	Dataset-3	Dataset-4
Blue	0.9576	0.9190	0.9338	0.9188
Green	0.9120	0.8956	0.9126	0.9146
Red	0.9230	0.9298	0.9215	0.9186
NIR	0.9654	0.9615	0.9196	0.8818

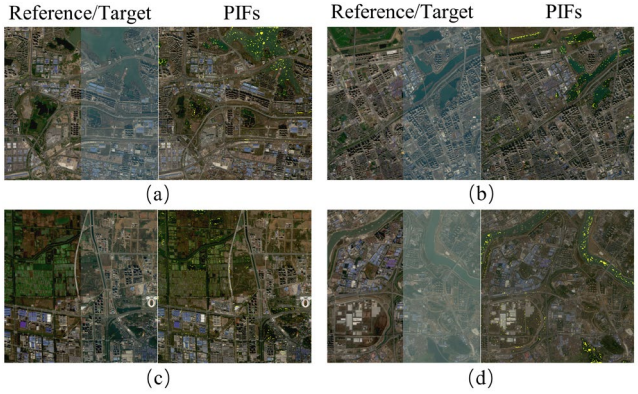

Fig. 2 Visualization of mosaicked reference/target images and PIFs of datasets 1-4 (a-d). The PIFs are displayed on the normalized target images.

TABLE III
PARAMETER SETTING OF MSOLG FEATURE EXTRACTION

mean r	N_o = 4	N_o = 6	N_o = 8	N_o = 10	N_o = 12
N_s = 2	0.9248	**0.9395**	0.9313	0.9226	0.9126
N_s = 3	0.9203	0.9343	0.9284	0.9280	0.9384
N_s = 4	0.9233	0.9350	0.9271	0.9247	0.9316
N_s = 5	0.9246	0.9381	0.9373	0.9337	0.9269

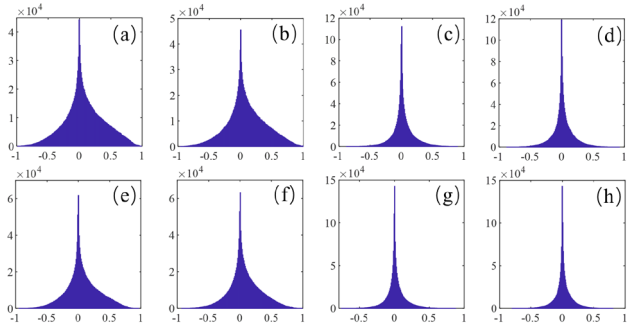

Fig. 3 Comparison of the histograms of raw SSIM (a-d) and weighted SSIM (e-h) yielded using the first four component pairs of MSOLG features.

C. Performance of RRN

Our PLS regression-based group-to-pixel modeling achieved high model precision on datasets 1-4, yielding an average R^2 of 0.90, 0.90, 0.87, and 0.84 and an average RMSE of 0.0189, 0.0142, 0.0262, and 0.0187.

The proposed RRN method effectively improved the brightness intensity differences and enhanced the radiometric consistency of the reference-target image pair, as evidenced by the following results. Fig. 4 showed that our RRN improved the color tone consistency of the image pair and resulted in more seamless cells. In terms of quantitative evaluations, our RRN significantly reduced the pixel differences of each band in the raw image pair (TABLE IV): the average $\mathrm{RMSE}_{\mathrm{Ave.}}{}^{b}$ of each dataset were decreased by 41.83%, 43.48%, 10.42%, and 57.01%. The enhanced radiometric consistency was also proven by the increased PSNR (dB): the average PSNR of each dataset was increased from the raw 24.92, 26.25, 26.30, and 23.80 to 28.34, 29.21, 28.24, and 28.69 (TABLE IV).

Multivariate regression-based modeling probably produces inaccurate transformations in the regions far from the majority of PIFs in the scatterplot, particularly in image pairs with significant radiometric differences due to factors such as cloud cover [4]. Although we mitigated these effects by identifying high-quality PIFs with a distribution across a wide range of pixel values [19] (Fig. 5), the impact on image pairs with significant radiometric distortion can be explored in future studies.

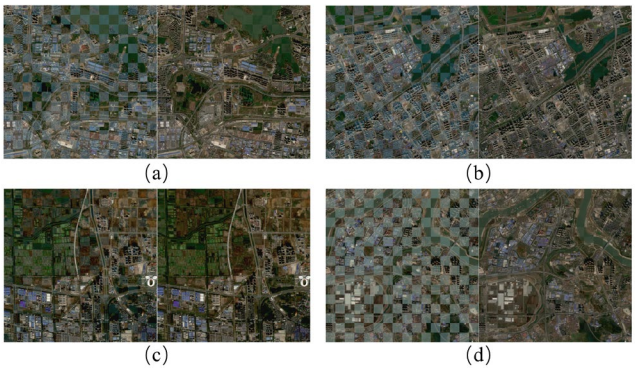

Fig. 4 Checkerboard visualization of datasets 1-4 (a-d) before (left) and after (right) performing RRN.

TABLE IV
QUANTITATIVE EVALUATION OF THE RRN PERFORMANCE

Dataset		RMSE of the unchanged pixels			PSNR	
		Raw	RRN	P_d/%	Raw	RRN
1	Blue	0.0615	0.0212	65.50	24.42	31.71
	Green	0.0496	0.0245	50.58	26.49	30.11
	Red	0.0364	0.0282	22.44	27.64	28.55
	NIR	0.0496	0.0353	28.83	21.14	22.98
2	Blue	0.0554	0.0195	64.76	26.04	31.95
	Green	0.0482	0.0216	55.33	27.47	30.52
	Red	0.0355	0.0240	32.31	28.49	29.14
	NIR	0.0435	0.0341	21.53	22.98	25.24
3	Blue	0.0333	0.0253	24.10	28.13	31.22
	Green	0.0310	0.0275	11.37	27.68	30.00
	Red	0.0317	0.0310	2.24	27.91	29.15
	NIR	0.0593	0.0569	3.95	21.50	22.60
4	Blue	0.0830	0.0161	80.57	22.74	31.18
	Green	0.0861	0.0185	78.52	22.52	30.28
	Red	0.0631	0.0215	66.01	25.24	28.50
	NIR	0.0437	0.0424	2.96	24.72	24.81

Note: P_d is the decreased percentage of the raw $\mathrm{RMSE}_{\mathrm{Ave.}}{}^{b}$.

D. Comparison of RRN methods

We compared the capability of our RRN method with six

prevalent methods on datasets 1-4. The comparative methods include HC, SR [1], IRMAD [5], ISFA [6], Speeded-up robust features (SURF)-based RRN [3], and Robust linear regression (RLR)-based pixel-to-pixel RRN using our PIFs. As shown in Fig. 6, our method outperformed the six comparative methods on all datasets with the lowest average $\mathrm{RMSE}_{\mathrm{Ave.}}{}^{b}$ of 0.0273, 0.0250, 0.0352, and 0.0246. The RLR-based normalization achieved secondary performance with the decreased average $\mathrm{RMSE}_{\mathrm{Ave.}}{}^{b}$ of 29.62%, 31.75%, 9.03%, and 49.30%. It proved the superiority of our method in identifying high-quality PIFs and producing an accurate RRN result using the group-to-pixel modeling strategy.

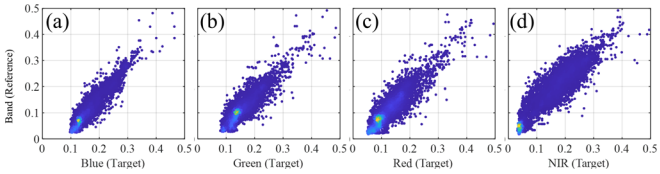

Fig. 5 Density scatterplot of PIFs in each band (a-d) of dataset 1.

	Raw	This study	RLR	HC	SR	IRMAD	ISFA	SURF
Dataset 1	0.0492	0.0273	0.0331	0.0379	0.0334	0.0331	0.0324	0.0328
Dataset 2	0.0457	0.025	0.0299	0.0337	0.0314	0.0326	0.0324	0.0304
Dataset 3	0.0388	0.0352	0.0359	0.0366	0.04	0.0394	0.0408	0.042
Dataset 4	0.069	0.0246	0.0287	0.0318	0.0311	0.0321	0.0356	0.0307

Fig. 6 Average $\mathrm{RMSE}_{\mathrm{Ave.}}{}^{b}$ of the unchanged pixels using different methods.

E. Method Applicability of Well-registered Images

Our RRN method was applicable for well-registered high- and mid-resolution images from the same sensor. For datasets 5-7, a total of 37,096, 28,552, and 9,047 pixels were identified as PIFs, with the mean r of 0.9058, 0.9566, and 0.8025. The application of RRN decreased average $\mathrm{RMSE}_{\mathrm{Ave.}}{}^{b}$ of each dataset from 0.0252, 0.0225, and 0.0355 to 0.0189, 0.0195, and 0.0188, resulting in the average P_d of 26.45%, 13.12%, and 44.66%. It also increased the mean PSNR of the image pair from 31.29, 32.15, and 26.57 to 33.46, 33.53, and 31.45.

IV. Conclusion

This letter introduced a multi-rule-based relative radiometric normalization for multi-sensor satellite images, including a spectral- and spatial-invariant PIFs identification method and a PLS-based group-to-pixel RRN modeling. The following effectiveness of our RRN method was validated on four multi-sensor datasets, including 1) identifying high-quality PIFs; 2) estimating precise RRN models for normalizing targets; 3) enhancing the radiometric consistency of the image pair. The comparison results with six prevalent RRN methods proved the superiority of our method in minimizing the radiometric differences of the image pair. The applicability validation results revealed that our method also performed well on well-registered high- and mid-resolution images of the same sensor.

References

[1] D. Yuan and C. D. Elvidge, "Comparison of relative radiometric normalization techniques," *ISPRS Journal of Photogrammetry and Remote Sensing,* vol. 51, no. 3, pp. 117-126, 1996/06/01/ 1996.

[2] F. G. Hall, D. E. Strebel, J. E. Nickeson, and S. J. Goetz, "Radiometric rectification: Toward a common radiometric response among multidate, multisensor images," *Remote Sensing of Environment,* vol. 35, no. 1, pp. 11-27, 1991/01/01/ 1991.

[3] A. Moghimi, T. Celik, A. Mohammadzadeh, and H. Kusetogullari, "Comparison of Keypoint Detectors and Descriptors for Relative Radiometric Normalization of Bitemporal Remote Sensing Images," *IEEE Journal of Selected Topics in Applied Earth Observations and Remote Sensing,* pp. 1-1, 2021.

[4] L. G. Denaro and C. H. Lin, "Hybrid Canonical Correlation Analysis and Regression for Radiometric Normalization of Cross-Sensor Satellite Imagery," *IEEE Journal of Selected Topics in Applied Earth Observations and Remote Sensing,* vol. 13, pp. 976-986, 2020.

[5] M. J. Canty and A. A. Nielsen, "Automatic radiometric normalization of multitemporal satellite imagery with the iteratively re-weighted MAD transformation," *Remote Sensing of Environment,* vol. 112, no. 3, pp. 1025-1036, 2008/03/18/ 2008.

[6] L. Zhang, C. Wu, and B. Du, "Automatic Radiometric Normalization for Multitemporal Remote Sensing Imagery With Iterative Slow Feature Analysis," *IEEE Transactions on Geoscience and Remote Sensing,* vol. 52, no. 10, pp. 6141-6155, 2014.

[7] W. Gan, H. Albanwan, and R. Qin, "Radiometric Normalization of Multitemporal Landsat and Sentinel-2 Images Using a Reference MODIS Product Through Spatiotemporal Filtering," *IEEE Journal of Selected Topics in Applied Earth Observations and Remote Sensing,* vol. 14, pp. 4000-4013, 2021.

[8] A. Moghimi, A. Mohammadzadeh, T. Celik, and M. Amani, "A Novel Radiometric Control Set Sample Selection Strategy for Relative Radiometric Normalization of Multitemporal Satellite Images," *IEEE Transactions on Geoscience and Remote Sensing,* vol. 59, no. 3, pp. 2503-2519, 2021.

[9] H. Xu, Y. Wei, X. Li, Y. Zhao, and Q. Cheng, "A novel automatic method on pseudo-invariant features extraction for enhancing the relative radiometric normalization of high-resolution images," *International Journal of Remote Sensing,* vol. 42, no. 16, pp. 6155-6186, 2021/08/18 2021.

[10] L. T. Huang, W. L. Jiao, T. F. Long, and C. L. Kang, "A RADIOMETRIC NORMALIZATION METHOD OF CONTROLLING NO-CHANGED SET (CNCS) FOR DIVERSE LANDCOVER USING MULTI-SENSOR DATA," *Int. Arch. Photogramm. Remote Sens. Spatial Inf. Sci.,* vol. XLII-3/W10, pp. 863-870, 2020.

[11] A. Moghimi, A. Sarmadian, A. Mohammadzadeh, T. Celik, M. Amani, and H. Kusetogullari, "Distortion Robust Relative Radiometric Normalization of Multitemporal and Multisensor Remote Sensing Images Using Image Features," *IEEE Transactions on Geoscience and Remote Sensing,* pp. 1-20, 2021.

[12] T. Kim and Y. Han, "Integrated Preprocessing of Multitemporal Very-High-Resolution Satellite Images via Conjugate Points-Based Pseudo-Invariant Feature Extraction," *Remote Sensing,* vol. 13, no. 19, 2021.

[13] A. Moghimi, T. Celik, and A. Mohammadzadeh, "Tensor-based keypoint detection and switching regression model for relative radiometric normalization of bitemporal multispectral images," *International Journal of Remote Sensing,* vol. 43, no. 11, pp. 3927-3956, 2022/06/03 2022.

[14] Y. Zhang, L. Yu, M. Sun, and X. Zhu, "A Mixed Radiometric Normalization Method for Mosaicking of High-Resolution Satellite Imagery," *IEEE Transactions on Geoscience and Remote Sensing,* vol. 55, no. 5, pp. 2972-2984, 2017.

[15] A. Höskuldsson, "PLS regression methods," *Journal of Chemometrics,* vol. 2, no. 3, pp. 211-228, 1988/06/01 1988.

[16] F. Thonfeld, H. Feilhauer, M. Braun, and G. Menz, "Robust Change Vector Analysis (RCVA) for multi-sensor very high resolution optical satellite data," *International Journal of Applied Earth Observation and Geoinformation,* vol. 50, pp. 131-140, 2016/08/01/ 2016.

[17] J. Li, Q. Hu, and M. Ai, "RIFT: Multi-Modal Image Matching Based on Radiation-Variation Insensitive Feature Transform," *IEEE Transactions on Image Processing,* vol. 29, pp. 3296-3310, 2020.

[18] W. R. Tobler, "A Computer Movie Simulating Urban Growth in the Detroit Region," *Economic Geography,* vol. 46, no. sup1, pp. 234-240, 1970/06/01 1970.

[19] Y. T. Solano-Correa, F. Bovolo, and L. Bruzzone, "Generation of Homogeneous VHR Time Series by Nonparametric Regression of Multisensor Bitemporal Images," *IEEE Transactions on Geoscience and Remote Sensing,* vol. 57, no. 10, pp. 7579-7593, 2019.